Electron precipitation from EMIC waves: a case study from 31 May 2013

Mark A. Clilverd[1], Roger Duthie[1], Rachael Hardman[1], Aaron T. Hendry[2], Craig J. Rodger[2], Tero Raita[3], Mark Engebretson[4], Marc R. Lessard[5], Donald Danskin[6], and David K. Milling[7]

[1] British Antarctic Survey (NERC), Cambridge, United Kingdom.

[2] Department of Physics, University of Otago, Dunedin, New Zealand.

[3] Sodankylä Geophysical Observatory, University of Oulu, Sodankylä, Finland.

[4] Department of Physics, Augsburg College, Minneapolis, Minnesota, USA.

[5] University of New Hampshire, Durham, New Hampshire, USA.

[6] Geomagnetic Laboratory, Natural Resources Canada, Ottawa, Canada.

[7] Department of Physics, University of Alberta, Edmonton, Canada.

Abstract.

On 31 May 2013 several rising-tone electromagnetic ion-cyclotron (EMIC) waves with intervals of pulsations of diminishing periods (IPDP) were observed in the magnetic local time afternoon and evening sectors during the onset of a moderate/large geomagnetic storm. The waves were sequentially observed in Finland, Antarctica, and western Canada. Co-incident electron precipitation by a network of ground-based Antarctic Arctic Radiation-belt Dynamic Deposition VLF Atmospheric Research Konsortia (AARDDVARK) and riometer instruments, as well as the Polar-orbiting Operational Environmental Satellite (POES) electron telescopes, was also observed. At the same time POES detected 30-80 keV proton precipitation drifting westwards at locations that were consistent with the ground-based observations, indicating substorm injection. Through detailed modelling of the combination of ground and satellite observations the characteristics of the EMIC-induced electron precipitation were identified as: latitudinal width of 2-3° or ΔL=1 R_{e}, longitudinal width ~50° or 3 hours MLT, lower cut off energy 280 keV, typical flux 1×10^{4} el. cm^{-2} sr^{-1} s^{-1} >300 keV. The lower cutoff energy of the most clearly defined EMIC rising tone in this study confirms the identification of a class of EMIC-induced precipitation events with unexpectedly low energy cutoffs of <400 keV.

1. Introduction

Electron precipitation driven by electro-magnetic ion-cyclotron (EMIC) waves in the Pc1-2 range (0.1-5 Hz) have been suggested as a significant loss mechanism for outer radiation belt fluxes of electrons in the 1-5 MeV energy range [*Millan and Thorne*, 2007]. Information about EMIC waves can be obtained from satellites [*Meredith et al.,* 2014], and by ground-based instrumentation [*Erlandson et al.*, 1996]. There are two principal regions where EMIC waves are found, close to the outer edge of the plasmasphere on the dusk-side of the Earth [*Fraser and Nguyen,* 2001], and also at high latitudes on the day-side [*Usanova et al.,* 2008]. The first group of EMIC waves, occurring near to the plasmapause, are at the right *L*-shells to interact with outer radiation belt electrons in the $3<L<6$ range and provide an electron loss pathway. Wave-particle cyclotron resonance interactions between the EMIC waves and <100 keV energy proton populations are likely to be ubiquitous, while under certain conditions anomalous cyclotron resonance may also drive electron precipitation into the atmosphere. However, although proton precipitation (30-80 keV) co-incident with EMIC wave occurrence has been observed [*Søraas et al*., 2005; *Sandanger et al.,* 2007], electron precipitation driven by EMIC waves has been much more difficult to characterise [e.g., *Rodger et al., 2008*].

Energetic electron precipitation has been associated with a subset of EMIC waves defined as Intervals of Pulsations with Diminishing Periods (IPDP). IPDP are observed in the evening sector during geomagnetically disturbed periods [*Yahnina et al., 2003* and references therein]. *Yahnina et al*. [2003] showed that the IPDP generation mechanism operates when newly injected protons drift westward, meeting a boundary of the dense plasmasphere such as the plasmapause or the plasmaspheric bulge region. The IPDP events were preceded by the injections of energetic protons (~100 keV) and were thus found to be related to substorm activity. The duration of IPDP events is typically shorter than other Pc1 wave types, with the duration being a few tens of minutes. NOAA POES Space Environment Monitor-1 (SEM-1) satellite observations of precipitating electrons from EMIC-IPDP waves showed enhanced fluxes in the >30 keV channel [*Yahnina et al.*, 2003], although we note that in an integral channel this may be caused by energies significantly higher than ~30 keV. However, the presence of the medium energy electrons is at odds with theoretical studies which suggest precipitation energies of ~1 MeV [*Thorne and Kennel*, 1971; *Kersten et al.,* 2014 and references therein], and do not account for potential proton contamination in the electron channel, which is now known to be significant for the POES Space Environment Monitor-2 (SEM-2) instrument [*Yando et al., 2011*].

At relativistic electron energies (>1 MeV) bursts of precipitation have been observed by SAMPEX and are commonly referred to as precipitation bands [*Blake et al.,* 1996]. The precipitation bands that occur during active geomagnetic conditions have been associated with EMIC waves [*Bortnik et al.,* 2006 and references therein]. The bands are detected in the afternoon-dusk sector during geomagnetic storms and have a correspondence with the radial location of the plasmapause [*Imhof et al.,* 1986]. Precipitation bands typically span a few degrees in latitude, and increase in magnitude and occurrence during the main phase of storms, particularly at *L*-shells consistent with the inner edge of the outer radiation belt (Blum, L., X. Li, and M. Denton (2015), Rapid MeV electron precipitation as observed by SAMPEX/HILT during high speed stream driven storms, submitted to J. Geophys. Res., 2014JA020633, 2015).

EMIC-driven energetic electron precipitation into the atmosphere has been detected using the technique of subionospheric radio-wave propagation by *Rodger et al.* [2008]. In that study *Rodger et al.* [2008] analysed a small group of events detected using subionospheric radio-wave propagation techniques to show that the electron precipitation events driven by EMIC-IPDP waves occurred close to the location of the dusk-side plasmapause (L~4.4) and during moderate geomagnetic activity (Kp~4). The electron precipitation was assumed to have a mono-energetic spectrum of ~2 MeV, partly to explain the subionospheric radiowave signatures, and partly to explain the lack of any riometer signatures. No satellite data was compared with the ground-based data shown.

Miyoshi et al. [2008] undertook a case study of electron precipitation using the POES SEM-2 telescopes. During a proton aurora that was observed from the ground in September 2005, POES flew through the region above and detected >800keV electron precipitation. Ground-based magnetometer data indicated the presence of hydrogen band EMIC waves with 0.5-0.9 Hz frequency. With a magnetic latitude that was close to the plasmapause at the time, both proton and electron precipitation were confirmed, but they had different latitudinal width in agreement with theoretical estimates made by *Jordanova et al.* [2007]. The observations were a clear confirmation that ions with energies of tens of keV can affect the evolution of relativistic electrons in the radiation belts via cyclotron resonance with EMIC waves.

Later, *Carson et al*. [2013] investigated the POES satellites SEM-2 dataset using an algorithm that identified EMIC-driven events when low energy (30-80 keV) proton precipitation was present at the same time as high energy electron precipitation (~1 MeV), and when no high energy proton precipitation was observed (which could cause false positive identifications). *Carson et al*. [2013] found that electron precipitation was observed on the dusk-side (16-02 MLT), and on or just outside of the plasmapause. The precipitation events were associated with periods of increased geomagnetic activity, and as showed an 11-year solar cycle dependence on the levels of geomagnetic activity, peaking during the declining phase when coronal interaction regions are most prevalent. However, no clear description could be made of the energy spectrum of the precipitation, or the size of the precipitation region (other than it being relatively narrow in *L*-shell). No ground-based data was compared with the satellite data shown.

Further analysis of the POES EMIC database showed two populations of precipitation event, one with a lower energy cutoff of >400 keV, and a second with <400 keV (A. T. Hendry, C. J. Rodger, M. A. Clilverd, T. Raita, Lower Energy cut-off limits of EMIC wave driven energetic electron precipitation, submitted to Geophysical Research Letters, 2015). The first type is predicted by anomalous cyclotron resonance [*Thorne and Kennel*, 1971; *Albert and Bortnik*, 2009], while the second type is predicted by non-resonant scattering [*Chen et al.*, 2014]. Rising tone hydrogen band EMIC waves can drive non-linear resonances with electrons as low as 500 keV [*Omura and Zhao*, 2013]. However, a simulation using CRRES EMIC wave power showed that only electron energies of >5 MeV would be lost from the radiation belts through precipitation into the atmosphere [*Kersten et al*., 2014]. Thus there is uncertainty in the published literature as to the mechanisms involved in EMIC-induced electron precipitation, as well as the range of electron energies that would be involved.

In this study we analyse in detail an 8 hour period of data during which EMIC waves were observed by three ground-based magnetometer sites, subionospheric radio-wave perturbations were seen at several AARDDVARK locations, and energetic electron precipitation events were detected by an EMIC-scattering algorithm applied to POES SEM-2 observations. The period analysed here is from 18:00 UT on 31 May 2013 until 02:00 UT on 01 June 2013. The observations are summarised, inter-comparisons made between instrument responses, and the energetic electron precipitation characteristics inferred. We confirm the previous observations of electron precipitation by EMIC-IPDP waves, provide an estimate of the lower cutoff of the electron energies involved, and determine the precipitation fluxes entering the atmosphere.

2. Experimental setup

To study the energetic electron precipitation fluxes into the atmosphere we use narrow band subionospheric very low frequency (VLF) and low frequency (LF) data spanning 19-38 kHz received sites that are part of the AARDDVARK network [*Clilverd et al.,* 2009; for further information see the description of the array at www.physics.otago.ac.nz/space/AARDDVARK_homepage.htm]. The subionospheric radio-waves come from VLF/LF transmitters that are stable in amplitude and frequency, and thus provide good quality signals for the analysis of perturbations caused by changes in the Earth-ionosphere waveguide driven by electron precipitation. Figure 1 shows the location of the transmitters (circles) and receivers (diamonds) involved in this study, as well the great circle subionospheric propagation paths between them. The propagation paths typically span the range 3<*L*<6, and are thus sensitive to electron precipitation driven by EMIC waves occurring close to the plasmapause, which is typically located at *L*~4-5 (indicated by contour lines on the map).

The EMIC wave observations are provided by three sites. In the northern hemisphere we make use of the Finnish array of pulsation magnetometers, focusing on the Oulu magnetometer located at *L*~4.4 [*Rodger et al*., 2008], and the CARISMA induction coil magnetometers, focusing on Fort Smith, Canada at *L*=6.8 [*Mann et al*., 2008]. In the southern hemisphere we use pulsation magnetometer data from Halley, Antarctica [*Engebretson et al.,* 2008], which is located at *L*~4.5. The approximate locations are shown in Figure 1 (blue squares). We concentrate on the frequency range of 0.1-1 Hz, in which Pc1-2, and IPDP waves are known to occur.

In this study we also make use of particle measurements by the SEM-2 instrument package onboard the POES spacecraft which are in Sun-synchronous orbits at ~800-850 km altitudes [*Evans and Greer*, 2004]. SEM-2 includes the Medium Energy Proton and Electron Detector (MEPED), in addition to the Total Energy Detector (TED). Together these instruments monitor electron fluxes from 50 eV up to 2700 keV. The POES SEM-2 instrument has been comprehensively described in *Rodger et al.* [2010] and so we will just note here that it provides measurements of the trapped and precipitating particle populations with 2 s time resolution. We use the algorithm described in *Carson et al.* [2013] to detect EMIC-driven precipitation during the study period, noting that *Carson et al.* were not able to unambiguously link the events detected in that study with ground-based signatures of EMIC waves, and thus defined their events as proton precipitation associated relativistic electron precipitation events (PPAREP).

3. Results

The background geomagnetic conditions for the period studied here are shown in Figure 2. The study period straddles the onset of a moderate/large geomagnetic disturbance, with Kp rising from 2 before 16 UT on 31 May to Kp~7 by 00-03 UT on 01 June 2013. Solar wind speed shows an increase at ~16 UT on 31 May, with a weak shock event seen at 15:32 UT by SOHO. The solar wind density rises gradually from ~16 UT, with high density values occurring towards the end of the day. During the actual study period shown in Figure 2 the solar wind speed, solar wind density, and geomagnetic activity levels remain relatively unchanging. However, the substorm index, A_L, [*Juusola et al.*, 2011] shows several features that could be substorm signatures occurring during the beginning of the study period, and we particularly note the one evident at ~20 UT on 31 May as a sharp decrease of ~130 nT followed by a gradual recovery lasting about 1 hour.

3.1 EMIC wave observations

Search coil magnetometer (SCM) observations from Oulu (Finland), Halley (Antarctica), and Fort Smith (Canada) from 18 – 24 UT on 31 May are shown in Figure 3. Wave power is shown over the frequency range 0-1 Hz. The main features that can be observed at all three sites are EMIC-IPDP waves, with elements rising from 0.1 to ~0.5 Hz. The IPDP features are initially seen at Oulu at ~2030 UT (~22 MLT), with Halley responding after 2100 UT (~1815 MLT), and Fort Smith further west responding after ~2130 UT (~1330 MLT). The IPDP features are significantly more distinct in the Halley data. We show Fort Smith data here (L~6.8) although we note that the L~4.5 site at Ministik Lake shows the same features at the same time as Fort Smith, but is less clearly identified because of local noise conditions. The frequency range over which the EMIC-IPDP waves are observed is appropriate for cyclotron resonance with O^+ band ions [*Engebretson et al.,* 2008]. This is consistent with previous observations of an increased generation of oxygen band EMIC waves during geomagnetic storms [*Bräysy et al.*, 1998].

The timing of the EMIC waves is potentially associated with the motion of low energy ions drifting westwards from an injection region near MLT midnight, crossing ~8.5 hours of MLT in about 1.5 hours, suggesting a drift period at *L*~4.5 of ~4.5 hours, and a proton energy of ~30-60 keV assuming a pitch angle of 45°. This proton energy is the energy expected to be involved in the generation of EMIC waves, with a drift motion expected for substorm injected protons from a nightside injection region [*Spasojevic and Fuselier,* 2009]. The occurrence of the substorm observed at ~20 UT in the AL index in Figure 2 is consistent with the observations presented here. As electrons injected during a substorm drift eastwards from the midnight injection region there is no expectation of any substorm-driven electron precipitation on the duskside, i.e., where we observe the EMIC waves, unless the EMIC waves are generating the electron precipitation themselves.

3.2 PPAREP observations

Figure 4 shows a map of the POES SEM-2 precipitating >300 keV electron fluxes for orbits which occurred during 21:15-22:00 UT on 31 May 2013. Enhanced fluxes can be seen in between the L=4 and L=5 contours shown on the map. The fluxes of >300 keV electrons within the contours are typically 1×10^4 el. cm^{-2} sr^{-1} s^{-1}. Using the algorithm developed by *Carson et al.* [2013] the POES SEM-2 dataset was analyzed over the same period. Several positive identifications of PPAREP events were made, and the insert of Figure 4 shows the L-shells and MLT values over-plotted on a cartoon of the wave-particle interaction regions adapted from *Summers et al*. [2007]. The events appear to be located in a range of MLT and occur on L-shells that are parallel to the plasmapause, consistent with the larger sample of events shown in *Carson et al*. [2013]. The events were observed at geographic longitudes that are similar to those ground-based sites shown in Figure 1, i.e., longitudes around the Weddell Sea region ranging from ~0° E to ~315° E in the southern hemisphere. The four events are clustered within ±15 minutes of 21:32 UT, but span an MLT range from 18-21 MLT, suggesting that a region covering ~3 hours in MLT is simultaneously experiencing electron precipitation.

Recent studies have extended the analysis of POES SEM-2 electron precipitation events identified by the *Carson et al.* [2013] algorithm (A. T. Hendry, C. J. Rodger, M. A. Clilverd, T. Raita, Lower Energy cut-off limits of EMIC wave driven energetic electron precipitation, submitted to Geophysical Research Letters, 2015). Using the calibrated, decontaminated, and integral POES electron precipitation flux measurements at >30, >100, >300 and >700 keV [*Yando et al.,* 2011] an energy spectrum and flux magnitude can be calculated for each event. Because of the integral flux measurements it is possible for all four of the SEM-2 channels to register enhanced fluxes, even if the energy distribution is limited to energies considerably higher than the nominal energy range for that channel. This could explain the observations of >30 keV EMIC-driven fluxes reported by *Yahnina et al.* [2003], although proton contamination is a possibility in that case [*Yando et al.,* 2011]. Of the four PPAREP events identified and plotted in Figure 1, three provided real solutions to the flux and spectral gradient calculations (A. T. Hendry, C. J. Rodger, M. A. Clilverd, T. Raita, Lower Energy cut-off limits of EMIC wave driven energetic electron precipitation, submitted to Geophysical Research Letters, 2015). The electron energy spectral gradient (*k*) of the EMIC-IPDP event at 21:30 UT was *k*=-2.3, with the lowest energy present given as 280 keV, and the highest as >5 MeV. In section 4.2 we will combine the PPAREP results for the 21:30 UT period with ground-based observations in order to provide further details about the EMIC-driven electron precipitation characteristics.

3.3 AARDDVARK observations

The AARDDVARK network has a large number of receivers, which typically record narrow-band signals from 10 or so transmitters [*Clilverd et al.,* 2009]. In this study we focus on individual paths that cover the *L*-shell ranges that pass under the magnetic field-line footprints of the plasmapause region (*L*~3-5). Figure 5 shows the phase and amplitude of the GVT transmitter (UK) received at Sodankylä, Finland during the study period. The non-disturbed amplitude and phase variation is represented by the dashed lines. Phase and amplitude variations are near non-disturbed levels until ~21 UT, when a large negative amplitude perturbation and a rapidly changing negative/positive phase perturbation, are observed, labeled (a). The characteristics of the amplitude perturbation are very similar to those previously reported by *Rodger et al.* [2008], i.e., an amplitude change of -12 dB associated with EMIC-drive electron precipitation on a UK-Finland path. We report, for the first time, the phase change of ~±25° observed with the EMIC event (indicated by red lines). Both the amplitude and the phase perturbations develop very quickly, reaching a maximum within 15 minutes of the first signs of deviation away from the non-disturbed levels. The geographic longitude range of the section of the GVT-SGO path that intersects the L=4 and L=5 contours (see Figure 1) is stated in Figure 5, indicating the longitude sector where the path is most likely to be responding to EMIC–driven electron precipitation [*Carson et al.,* 2013].

The phase data from four additional paths are presented in Figure 6. The format of the panels is the same as for Figure 5. The panels represent paths that are shown in Figure 1, and perturbations are labeled (a) – (d) in time ascending order. The longitude range of the section of the path intersecting L=4-5 is shown, with the top-left panel (GVT, UK to Ny Ålesund, Svalbard) being the most easterly path, and the bottom-right panel (NPM, Hawaii to Halley, Antarctica) the most westerly. However, because the NPM-Halley propagation path lies within the L=4 and L=5 contours for ~100° of longitude to the west of Halley, the integrated phase effect along that bit of the path makes perturbation (c) by far the largest event of the four. Perturbation (a), co-incident with the EMIC wave seen at Oulu at 21:00 UT, is observed in all panels other than NPM-Halley, suggesting that electron precipitation is occurring over a longitude range of 55±10°, i.e., from Europe (14-25°E) to the Atlantic south of Greenland (320-340°E), but not further west. The phase perturbation is typically 25° in each of the paths. Perturbations (b), (c), and (d) are only observed on some of the paths. The NRK, Iceland to St. John's, Newfoundland path is unusual in that it shows all of the perturbations, including perturbation (b) at 21:30 UT, which is the time of the first strong IPDP EMIC wave seen at Halley, and also the time of the POES-identified PPRAREP signatures. We note here that the conjugate point of Halley is close to the NRK, Iceland to St. John's, Newfoundland path as shown in Figure 1 by the yellow triangle.

Analysis of the NLK-Churchill subionospheric path (see Figure 1) indicates a clear phase perturbation at 22:00 UT (not shown). This timing is consistent with the start of the IPDP activity seen at Ministik Lake/Fort Smith in western Canada. As shown in Figure 1, the NLK-Churchill propagation path passes close to the Ministik site, and together they confirm the suggestion of an IPDP-induced precipitation region moving westwards.

The time variation of the Halley SCM Pc1-2 wave power in the range 0.05-0.5 Hz, the Halley riometer absorption, and the NRK-St. John's phase perturbation for the study period are shown in Figure 7. We use NRK-St. John's due to the similarity of the longitude range at L=4-5 compared with that of Halley. Vertical lines indicate the same times as in previous figures along with the same labeling given to features in the panels. Both the SCM and riometer measurements are made essentially overhead of the detectors at Halley (with fields of view that are 100s of km, centered on the instrument), while the NRK-St. John's path responds to propagation conditions in the region conjugate to Halley as shown in Figure 1. Thus it would appear from Figure 7 that perturbation (a) is not observable from Halley on any instrument, while perturbation (b) is seen by the SCM and riometer and therefore must be close to Halley or just to the east. Perturbation (c) at 22:45 UT is observed west and east of Halley in the AARDDVARK data, overhead at Halley in the riometer data, but does not have a clear association with any specific EMIC wave feature at Oulu or Halley. Perturbation (d) is clearly observed in the riometer data overhead of Halley, also in the conjugate AARDDVARK data, and appears to be associated with an increase in Pc1-2 wave power observed at Oulu and Halley. However the broadband nature of the Pc1-2 wave power (as shown in Figure 3) is not consistent with EMIC wave activity but more suggestive of a geomagnetic disturbance. However, although only some specific features coincide in the data plotted in Figure 7, there is overall similarity in all of the panels where the Halley SCM, riometer absorption, and AARDDVARK phase perturbation data show increased activity levels from ~21:30 UT lasting until ~00:30 UT the next day.

4. Calculating EMIC-driven electron precipitation characteristics

Using the Long Wave Propagation Code [LWPC, *Ferguson and Snyder*, 1990] we have calculated the VLF wave propagation from the transmitters of interest to their respective receivers. In LWPC the transmitted wave propagates in the Earth-ionosphere waveguide, with the lower boundary given by a surface conductivity map. The upper boundary condition is provided by a D-region electron density altitude-profile. We use a Wait ionosphere where the electron number density (i.e., electrons per m^3), N_e, increases exponentially with altitude *z,* and is defined in terms of a sharpness parameter β and a reference height h' [*Wait and Spies*, 1964]. The β and h' of the ambient ionosphere is provided by the analysis of *Thomson et al.* [2007], *Thomson and McRae* [2009], and *Thomson et al.* [2011] and depends on the time of day being modeled.

Initially, complete days of observations were compared with the LWPC output, in order to give confidence that the D-region modeling parameters (β and h') were appropriate for each path. Then β and h' were systematically varied over the part of the path that spanned L=4 – 5 during the time of the EMIC event, i.e., ΔL=1, in order to compare the calculated phase and amplitude changes with the observed perturbation values on 31 May 2013. The latitudinal separation between L=4 and L=5 contours is about 3°, which is consistent with the width of EMIC precipitation bands observed by SAMPEX (Blum, L., X. Li, and M. Denton (2015), Rapid MeV electron precipitation as observed by SAMPEX/HILT during high speed stream driven storms, submitted to J. Geophys. Res., 2014JA020633, 2015). The β and h' of the rest of the path were kept the same as the non-disturbed case.

4.1 Analysis of event (a)

Figure 8 shows the comparison between LWPC calculations and the GVT-Sodankylä observations on 30 May 2013, which we use as a representative non-disturbed day. In both of the phase and amplitude panels the observed values are indicated by the solid line, while the LWPC results are represented by the diamonds.

A vertical dashed line indicates 21:00 UT, which is the time of the EMIC-driven perturbation shown in Figure 5. The panels show that the LWPC modeling is capturing the non-disturbed diurnal variation in phase and amplitude, and that at 21:00 UT the LWPC background β and h' values should be representative of the undisturbed ionosphere. The phase value at 21:00 UT also suggests that the propagation path can be considered to be day lit, as the decrease towards typical nighttime values has not started at that time. The lower two panels show the variation of the phase and amplitude perturbations from the non-disturbed values as β and h' are varied within a range that is expected to occur as a result of electron precipitation. The initial non-disturbed values of β and h' were β=0.32 km^{-1} and h'=76 km. At 21:00 UT the GVT amplitude shown in Figure 5 is perturbed by -12 dB, at the same time the phase rapidly changes from a perturbation of -25° to +25° (indicated by red lines). The two lower panels of Figure 8 indicate that these conditions are met when h'=~64 km, although it is unclear which β value is most appropriate. Similar analysis (not shown) of the other three northern hemisphere paths that respond to the electron precipitation associated with this event also suggest h'=64 ± 1 km at the peak of the event, but also provide little β information. This analysis therefore indicates that EMIC-driven precipitation has lowered the reference altitude from ~76 km to ~64 km, but it is unclear what exact electron density profile exists around that altitude. At 64 km the most likely energy of electron precipitation that would produce excess ionization is ~300 keV [*Turunen et al.,* 2008].

4.2 Analysis of event (b)

The second EMIC-IPDP event occurs at 21:30 UT and is observed by the magnetometer and riometer instruments at Halley, and the AARDDVARK path that passes close to the Halley conjugate location in the northern hemisphere (NRK-St. John's). The Halley AARDDVARK data from NPM Hawaii shows only an onset of disturbance in phase and amplitude at 21:30 UT rather than a peak in effect, although this is consistent with electron precipitation initially only influencing a small part of the 13,387 km long propagation path, i.e., electron precipitation only occurring overhead of Halley at that time and not to the west. Using LWPC as before, we find that the NRK-St. John's phase perturbation of ~40° (as shown in Figure 6) is reproduced by an *h'*=64 km, consistent with electron precipitation energies of ~300 keV.

We can combine the information gained from the AARDDVARK observations, Halley riometer, and the POES SEM-2 precipitation channels to investigate this event more closely. Using the energy spectrum information given by POES as described in section 3.2 we can model the electron density profile that would be generated overhead of the Halley riometer. We do this using the ionosphere model described in *Rodger et al*. [2012]. Figure 9 (left hand panel) shows the results from the calculations, where the flux of electron precipitation with an energy spectrum of *k*=-2.3 and an energy range of 280 keV to 5 MeV was varied over a wide range of flux values and the resulting 30 MHz riometer absorption calculated following the method described in *Rodger et al*. [2012]. The observed absorption value of 0.4 dB is highlighted by a green circle and is generated by an electron flux of 1 x 10^4 el. cm^{-2} s^{-1} sr^{-1}. This flux level is consistent with the observed fluxes reported by POES during the event. The right hand panel shows electron density profiles for the ambient D-region profile (black line) and the profile that would be generated by the precipitation required to give 0.4 dB riometer absorption in the left hand panel (ΔCNA, red line). The background D-region profile is given by a combination of nighttime β and h' values [*Thomson et al., 2007*] and the IRI model, again following the techniques described in *Rodger et al.* [2012]. Blue lines show two electron density profiles based on Wait ionospheres defined by β and h' values as labeled. Over the altitude range that the reflection of oblique VLF waves would be occurring (50-70 km) there is good agreement between the ΔCNA profile and h' = 63-64 km, $\beta = 0.3$ km^{-1}. The h' of the ΔCNA profile confirms the h' found by analysis of the AARDDVARK phase and amplitude perturbations (h'=64 ± 1). In addition, the analysis suggests that $\beta = 0.3$ km^{-1} is the most likely value for the sharpness parameter – something that the analysis of the AARDDVARK data was unable to determine accurately in this study.

Thus we have shown that an EMIC-IPDP wave in the oxygen band is capable of precipitating electrons with energies as low as ~300 keV. A distinct population of events with this sort of unusually low lower-energy cutoff has recently been found, where the population occurred ~20% of the time in an extensive database of EMIC events (A. T. Hendry, C. J. Rodger, M. A. Clilverd, T. Raita, Lower Energy cut-off limits of EMIC wave driven energetic electron precipitation, submitted to Geophysical Research Letters, 2015). *Saikin et al.* [2014] undertook a statistical study of EMIC waves observed by the Van Allen Probes mission, and found that oxygen band waves occurred in ~11-13% of EMIC events. Although the MLT distribution of oxygen band EMIC waves observed by *Saikin et al.* [2014] shows no preference towards the evening sector position seen here, it may be that the low cutoff energy population (<400 keV) is preferentially caused by Oxygen band EMIC waves.

4.3 Analysis of events (c) and (d)

The largest phase perturbation occurs during events (c) and (d) on two of the AARDDVARK paths, peaking at 22:45 UT on the NRK-St. John's path close to the Halley conjugate location, and on the NPM-Halley path looking west of Halley. The Halley riometer also shows a distinct peak in absorption at about 22:45-23:00 UT, with the largest absorption value observed during the study period (0.5 dB). Phase perturbations of ~25° on the GVT-Ny Ålesund path, ~50° on the NRK-St. John's path, and 280° on the NPM-Halley path, are modeled by LWPC with *h'*=64 -65 km, and in the case of NPM-Halley β=0.6 km^{-1}. The reason why the NPM-Halley path has such a large phase perturbation compared with the other paths is due to the large part of the propagation path that lies within the *L*=4-5 contours (see Figure 1), consistent with the LWPC modeling assuming that the whole of that part of the path is affected by electron precipitation. However, the interpretation of event (c) is more difficult than for (a) and (b). Observations suggest that overhead, as well as east and west, of Halley longitudes (and Halley conjugate longitudes), electron precipitation fluxes were increasing following a recovery from event (b) at 21:30 UT. At 22:45 UT almost all observations made in the longitude range studied here (>120°) shows a peak of response. However, no clear EMIC wave can be identified, and

Figures 3 and 7 suggest that EMIC wave power, although elevated, is actually decreasing at the time. Thus if EMIC-driven precipitation does occur around 22:45 UT it is likely to be contributing to only a fraction of the perturbation levels observed, and another process is acting as well.

Event (d) is also observed by the riometer at Halley with an absorption level of 0.5 dB, and on the NRK-St. John's AARDDVARK path, as a short-lived, sharp-peaked phase perturbation. However, both search coil magnetometers at Halley and Oulu suggest that the event is only accompanied by broadband Pi1-Pi2 wave power, and thus is not an EMIC wave event. The electron precipitation seems localized to Halley and Halley conjugate longitudes, but the driving mechanism is unclear, although the occurrence of strong Pi1-Pi2 ULF noise and co-incident riometer absorption is consistent with the onset of a geomagnetic storm [*Engebretson et al.,* 2008].

5. Discussion and Summary

During the onset of a moderate geomagnetic storm several rising-tone EMIC-IPDP waves were observed in the evening sector with co-incident detection of electron precipitation by ground-based AARDDVARK and riometer instruments. At the same time the POES SEM-2 particle precipitation telescopes detected 30-80 keV proton and 280-5000 keV electron precipitation at locations that were consistent with the ground-based observations. The latitude of the electron precipitation is consistent with the location of the evening sector plasmapause (L~4). The detection of electron precipitation occurred in an east to west order in both hemispheres, consistent with the drift of 30-80 keV substorm protons injected close to magnetic midnight and drifting westwards.

Through a combination of ground and satellite observations the characteristics of the electron precipitation were identified as:

- Latitudinal width of 2-3° or ΔL=1 R_e
- Longitudinal width of ~50° or 3 hours MLT
- Lower cut off energy of 280 keV
- Upper cut off energy of >5 MeV
- Typical flux 1×10^4 el. cm^{-2} sr^{-1} s^{-1} >300 keV

We find that the lower cutoff energy of the most clearly defined EMIC rising tone in this study is in the class of events with cutoff <400 keV as described by recent work (A. T. Hendry, C. J. Rodger, M. A. Clilverd, T. Raita, Lower Energy cut-off limits of EMIC wave driven energetic electron precipitation, submitted to Geophysical Research Letters, 2015). The presence of electron precipitation with energies of ~300 keV is confirmed through detailed modelling of observed riometer and AARDDVARK radiowave perturbations. The Oxygen band rising tone EMIC-IPDP waves observed here appear to generate electron precipitation at lower energies than predicted through anomalous resonance, and instead, suggest non-resonant scattering processes could be occurring.

Acknowledgements. The authors would like to thank Bergur Helgi and Jon Bjorn Richardsson for their assistance and enthusiasm during the data collection in Iceland. Data for this paper are available at the British Antarctic Survey Polar Data Centre (http://psddb.nerc-bas.ac.uk/data/access/). MAC would like to acknowledge support from the Natural Environmental Research Council grant NE/J008125/1. AH, RD and RH received funding from the European Community's Seventh Framework Programme ([FP7/2007-2013]) under grant agreement number 263218. CARISMA is operated by the University of Alberta and funded by the Canadian Space Agency. Support for the Halley search coil magnetometer was provided by U.S. National Science Foundation grants PLR-1341493 to Augsburg College and PLR-1341677 to the University of New Hampshire.

References

Albert, J., and J. Bortnik (2009), Nonlinear interaction of radiation belt electrons with electromagnetic ion cyclotron waves, Geophys. Res. Lett., 36 (12).

Blake, J. B., M. D. Looper, D. N. Baker, R. Nakamura, B. Klecker, and D. Hovestadt (1996), New high temporal and spatial resolution measurements by SAMPEX of the precipitation of relativistic electrons. Adv. Space Res., 18(8), 171-186.

Bortnik, J., R. M. Thorne, T. P. O'Brien, J. C. Green, R. J. Strangeway, Y. Y. Shprits, and D. N. Baker (2006), Observation of two distinct, rapid loss mechanisms during the 20 November 2003 radiation belt dropout event, J. Geophys. Res., 111, A12216, doi:10.1029/2006JA011802.

Braysy, T., K. Mursula, and G. Marklund (1998), Ion cyclotron waves during a great magnetic storm observed by Freja double-probe electric field instrument, J. Geophys. Res., 103(A3), 4145–4155, doi:10.1029/97JA02820.

Carson, B. R., C. J. Rodger, and M. A. Clilverd (2013), POES satellite observations of EMIC-wave driven relativistic electron precipitation during 1998–2010, J. Geophys. Res., 118, 232–243, *doi:*10.1029/2012JA017998.

Chen, L., R. M. Thorne, and J. Bortnik (2014), Non-resonant interactions of electromagnetic ion cyclotron waves with relativistic electrons, J. Geophys. Res., In Press.

Clilverd, M. A., C. J. Rodger, N. R. Thomson, J. B. Brundell, Th. Ulich, J. Lichtenberger, N. Cobbett, A. B. Collier, F. W. Menk, A. Seppälä, P. T. Verronen, and E. Turunen (2009), Remote sensing space weather events: the AARDDVARK network, Space Weather, 7, S04001, doi:10.1029/2008SW000412.

Engebretson, M. J., et al. (2008), Pc1–Pc2 waves and energetic particle precipitation during and after magnetic storms: Superposed epoch analysis and case studies, J. Geophys. Res., 113, A01211, doi:10.1029/2007JA012362.

Erlandson, R. E., K. Mursula, and T. Bosinger (1996), Simultaneous ground-satellite observations of structured Pc-1 pulsations, J. Geophys. Res., 101, 27149-27156.

Evans, D. S., and M. S. Greer (2004), Polar Orbiting environmental satellite space environment monitor - 2 instrument descriptions and archive data documentation, NOAA technical Memorandum version 1.4, Space Environment Laboratory, Colorado.

Ferguson, J. A., and F. P. Snyder (1990), Computer programs for assessment of long wavelength radio communications, Tech. Doc. 1773, Natl. Ocean Syst. Cent., San Diego, California.

Fraser, B. J. and Nguyen, T. S. (2001), Is the plasmapause a preferred source region of electromagnetic ion cyclotron waves in the magnetosphere?, J. Atmos. Solar-Terr. Phys., 63, 1225–1247.

Imhof, W.L., H.D. Voss, J.B. Reagan, D.W. Datlowe, E.E. Gaines, J. Mobilia (1986), Relativistic electron and energetic ion precipitation spikes near the plasmapause, J. Geophys. Res., 91, 3077–3088.

Jordanova, V. K., M. Spasojevic, and M. F. Thomsen (2007), Modeling the electromagnetic ion cyclotron wave-induced formation of detached subauroral proton arcs, J. Geophys. Res., 112, A08209, doi:10.1029/2006JA012215.

Juusola, L., N. Østgaard, E. Tanskanen, N. Partamies, and K. Snekvik (2011), Earthward plasma sheet flows during substorm phases, J. Geophys. Res., 116, A10228, doi:10.1029/2011JA016852.

Kersten, T., R. B. Horne, S. Glauert, N. P. Meredith, B. J. Fraser, and R. S. Grew (2014), Electron losses from the radiation belts caused by EMIC waves, J. Geophys. Res., In Press.

Mann, I.R., et al., (2008), The upgraded CARISMA magnetometer array in the THEMIS era, Space Sci. Rev., 141, 413-451, doi: 10.1007/s11214-008-9457-6.

Meredith, N. P., R. B. Horne, T. Kersten, B. J. Fraser, and R. S. Grew (2014), Global morphology and spectral properties of EMIC waves derived from CRRES observations, J. Geophys. Res. Space Physics, 119, 5328–5342, doi:10.1002/2014JA020064.

Millan, R. M., and R. M. Thorne (2007), Review of radiation belt relativistic electron loss, J. Atmos. Sol. Terr. Phys., 69, 362–377, doi:10.1016/j.jastp.2006.06.019.

Miyoshi, Y., K. Sakaguchi, K. Shiokawa, D. Evans, J. Albert, M. Connors, and V. Jordanova (2008), Precipitation of radiation belt electrons by EMIC waves, observed from ground and space, Geophys. Res. Lett., 35, L23101, doi:10.1029/2008GL035727.

Omura, Y., and Q. Zhao (2013), Relativistic electron microbursts due to nonlinear pitch angle scattering by emic triggered emissions, Journal of Geophysical Research, 118 (8), 5008-5020.

Rodger, C. J., T. Raita, M. A. Clilverd, A. Seppälä, S. Dietrich, N. R. Thomson, and T. Ulich (2008), Observations of relativistic electron precipitation from the radiation belts driven by EMIC waves, Geophys. Res. Lett., 35 (16), doi:10.1029/2008GL034804.

Rodger, C. J., M. A. Clilverd, J. Green, and M.-M. Lam (2010), Use of POES SEM-2 observations to examine radiation belt dynamics and energetic electron precipitation in to the atmosphere, J. Geophys. Res., 115, A04202, doi:10.1029/2008JA014023.

Rodger, C. J., M. A. Clilverd, A. J. Kavanagh, C. E. J. Watt, P. T. Verronen, and T. Raita (2012), Contrasting the responses of three different ground-based instruments to energetic electron precipitation, Radio Sci., 47(2), RS2021, doi:10.1029/2011RS00497.

Saikin, A. A., J. -C. Zhang, R.C. Allen, C. W. Smith, L. M. Kistler, H. E. Spence, R. B. Torbert, C. A. Kletzing, and V. K. Jordanova (2014), A statistical study of hydrogen-, helium-, and oxygen-band EMIC waves observed by Van Allen Probe A, GEM Summer Workshop, Portsmouth, VA, 15-20, 53.

Sandanger, M., F. Søraas, K. Aarsnes, K. Oksavik, and D. S. Evans (2007), Loss of relativistic electrons: Evidence for pitch angle scattering by electromagnetic ion cyclotron waves excited by unstable ring current protons, J. Geophys. Res., 112 (A12), doi:10.1029/2006JA012138.

Søraas, F., K. Aarsnes, D. Carlsen, K. Oksavik, and D. Evans (2005), Ring Current Behavior as Revealed by Energetic Proton Precipitation, Washington DC American Geophysical Union Geophysical Monograph Series, 155, 237.

Spasojevic, M., *and* S. A. Fuselier (2009), Temporal evolution of proton precipitation associated with the plasmaspheric plume, J. Geophys. Res., 114, *A12201, doi:*10.1029/2009JA014530.

Summers, D., B. Ni, and N. P. Meredith (2007), Timescales for radiation belt electron acceleration and loss due to resonant wave-particle interactions: 2. Evaluation for VLF chorus, ELF hiss, and electromagnetic ion cyclotron waves, J. Geophys. Res., 112, A04207, doi:10.1029/2006JA011993.

Thomson, N. R., M. A. Clilverd, and W. M. McRae (2007), Nighttime ionospheric D region parameters from VLF phase and amplitude, J. Geophys. Res., 112, A07304, doi:10.1029/2007JA012271.

Thomson, N. R., and W. M. McRae (2009), Nighttime ionospheric D region: Equatorial and nonequatorial, J. Geophys. Res., 114, A08305, doi:10.1029/2008JA014001.

Thomson, N. R., M. A. Clilverd, and C. J. Rodger (2011), Daytime midlatitude D region parameters at solar minimum from short-path VLF phase and amplitude, J. Geophys. Res., 116, A03310, doi:10.1029/2010JA016248.

Thorne, R. M., and C. F. Kennel (1971), Relativistic electron precipitation during magnetic storm main phase, J. Geophys. Res. Space Physics, 76, 4446-4453.

Turunen, E., P. T. Verronen , A. Seppälä, C. J. Rodger, M. A. Clilverd, J. Tamminen, C.-F. Enell, and Th. Ulich (2008), Impact of different precipitation energies on NOx generation during geomagnetic storms, J. Atmos. Sol.-Terr. Phys., 71 (10), 1176-1189.

Usanova, M. E., I. R. Mann, I. J. Rae, Z. C. Kale, V. Angelopoulos, J. W. Bonnell, K. H. Glassmeier, H. U. Auster, and H. J. Singer (2008), Multipoint observations of magnetospheric compression-related EMIC Pc1 waves by THEMIS and CARISMA, Geophys. Res. Lett., 35 (17), doi:10.1029/2008GL034458.

Wait, J. R., and K. P. Spies (1964), Characteristics of the Earthionosphere waveguide for VLF radio waves, NBS Tech. Note 300, Natl. Bur. of Stand., Gaithersburg, Md.

Yahnina, T. A., A. G. Yahnin, J. Kangas, J. Manninen, D. S. Evans, A. G. Demekhov, V. Y. Trakhtengerts, M. F. Thomsen, G. D. Reeves, and B. B. Gvozdevsky (2003), Energetic particle counterparts for geomagnetic pulsations of Pc1 and IPDP types, Ann. Geophys., **21**, 2281–2292.

Yando, K., R. M. Millan, J. C. Green, and D. S. Evans (2011), A Monte Carlo simulation of the NOAA POES Medium Energy Proton and Electron Detector instrument, J. Geophys. Res., 116, A10231, doi:10.1029/2011JA016671.

M. A. Clilverd, R Duthie, R. Hardman, British Antarctic Survey, High Cross, Madingley Road, Cambridge CB3 0ET, England, U.K. (email: macl@bas.ac.uk)

D. Danskin, Geomagnetic Laboratory, Natural Resources Canada, Ottawa, Canada. (email: Donald.Danskin@NRCan-RNCan.gc.ca)

M. Engebretson, Augsberg College, 2211 Riverside Ave. Minneapolis, MN 55454, USA. (email: engebret@augsburg.edu)

A. Hendry, C. J. Rodger, Department of Physics, University of Otago, P.O. Box 56, Dunedin, New Zealand. (email: crodger@physics.otago.ac.nz).

M. R. Lessard, Magnetosphere-Ionosphere Research Lab, Institute for the Study of Earth, Oceans, and Space, University of New Hampshire, Durham, NH, USA. (email: marc.lessard@unh.edu)

D. K. Milling, Department of Physics, University of Alberta, Edmonton, AB, Canada T6G 2E1. (email: dmilling@ualberta.ca)

T. Raita, Sodankylä Geophysical Observatory, University of Oulu, Sodankylä, Finland. (email: tero.raita@sgo.fi)

(Received N x, 2015 N x 27, 2015

accepted N x, 2015)

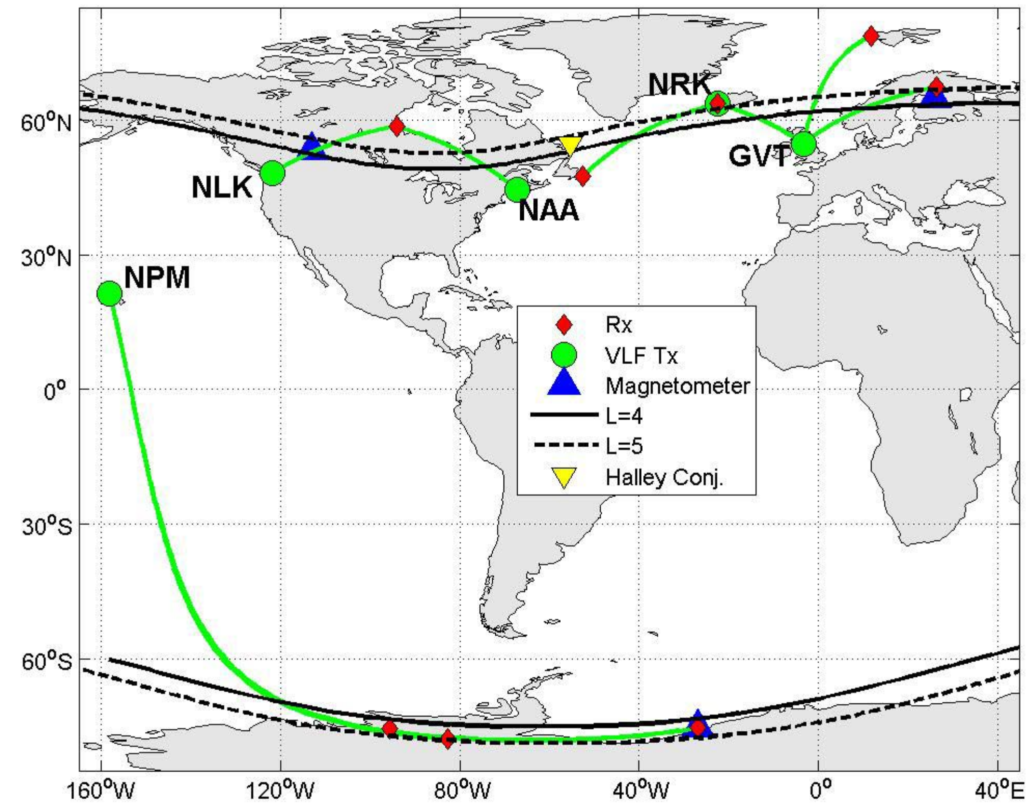

Figure 1. The locations of the main subionospheric propagation paths from the AARDDVARK network analyzed for the effects of EMIC-driven electron precipitation on 31 May 2013. The great circle paths (green lines) connect transmitters (green circles) to receivers (red diamonds). Search coil magnetometer locations are indicated by blue triangles. Constant L-shell contours at 100 km altitude are shown as solid (L=4) and dashed (L=5) black lines.

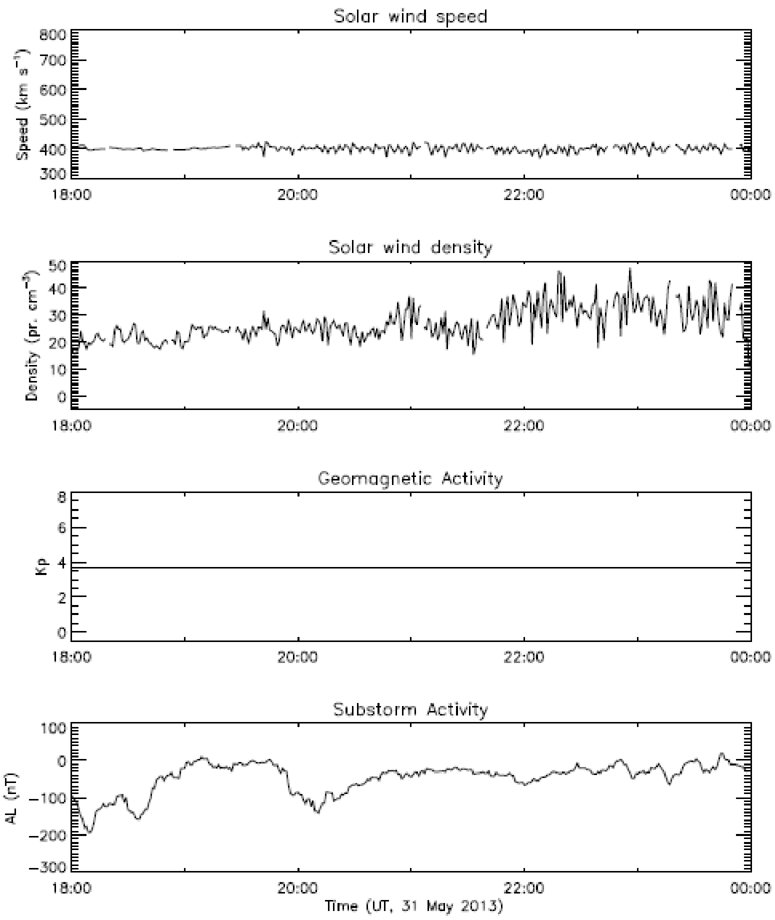

Figure 2. Geomagnetic conditions for 18-00 UT, 31 May 2013, during the onset of a geomagnetic disturbance late on 31 May. The solar wind speed, solar wind density, geomagnetic activity index Kp, and substorm index A_L are plotted in separate panels.

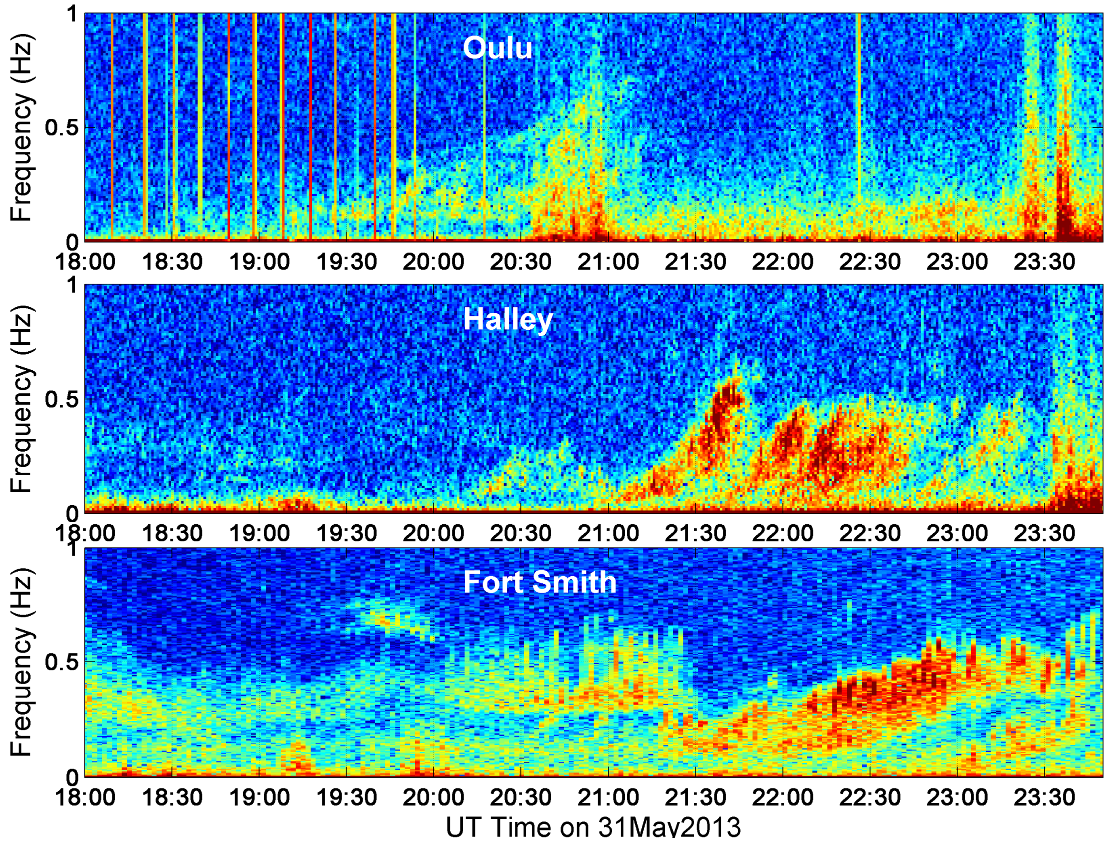

Figure 3. Pulsation magnetometer data from Oulu, Finland (MLT = UT + 1:30), Halley, Antarctica (MLT = UT - 2:44), and Fort Smith, Canada (MLT=UT – 8:07) from 18 – 24 UT, 31 May 2013. The color scale represents the Pc1-Pc2 wave power (arbitrary units) in the 0.1-1 Hz frequency range. Intervals of pulsations of diminishing periods (IPDPs) are observed at all three sites, arriving later at the more westward locations (in the order Oulu-Halley-Fort Smith).

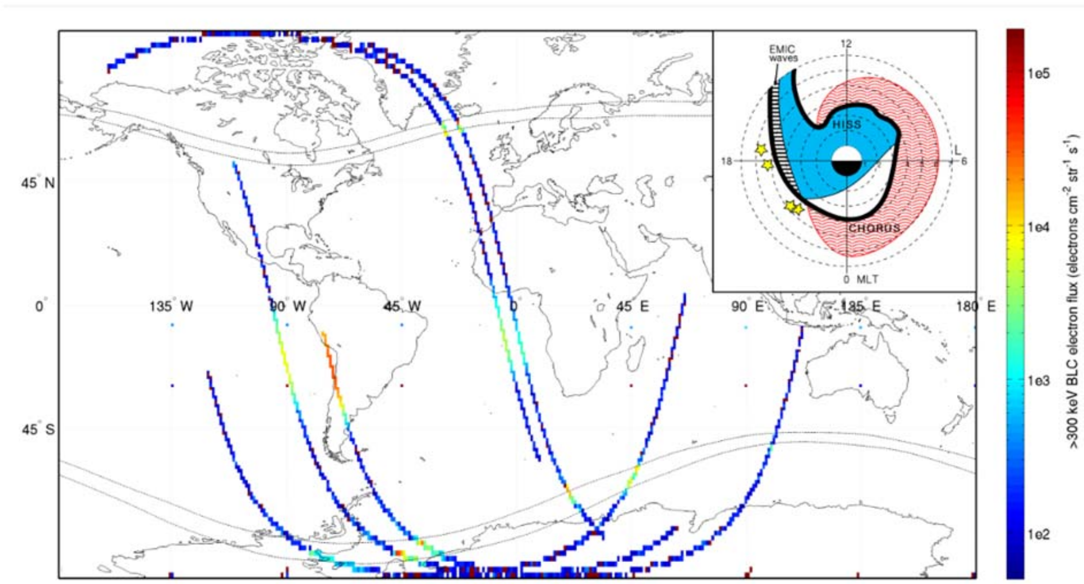

Figure 4. A map of the orbits of POES satellites during 21:15-22:00 UT on 31 May 2013. The color scale represents the >300 keV precipitating electron flux. Contours of *L*=4 and *L*=5 are shown by dashed lines. Insert. The MLT and L-shell of relativistic electron precipitation events observed by POES at about 21:30 UT on 31 May 2013. Super-imposed on this map is a cartoon representation of the plasmasphere and wave dominated regions, described by *Summers et al.* [2007].

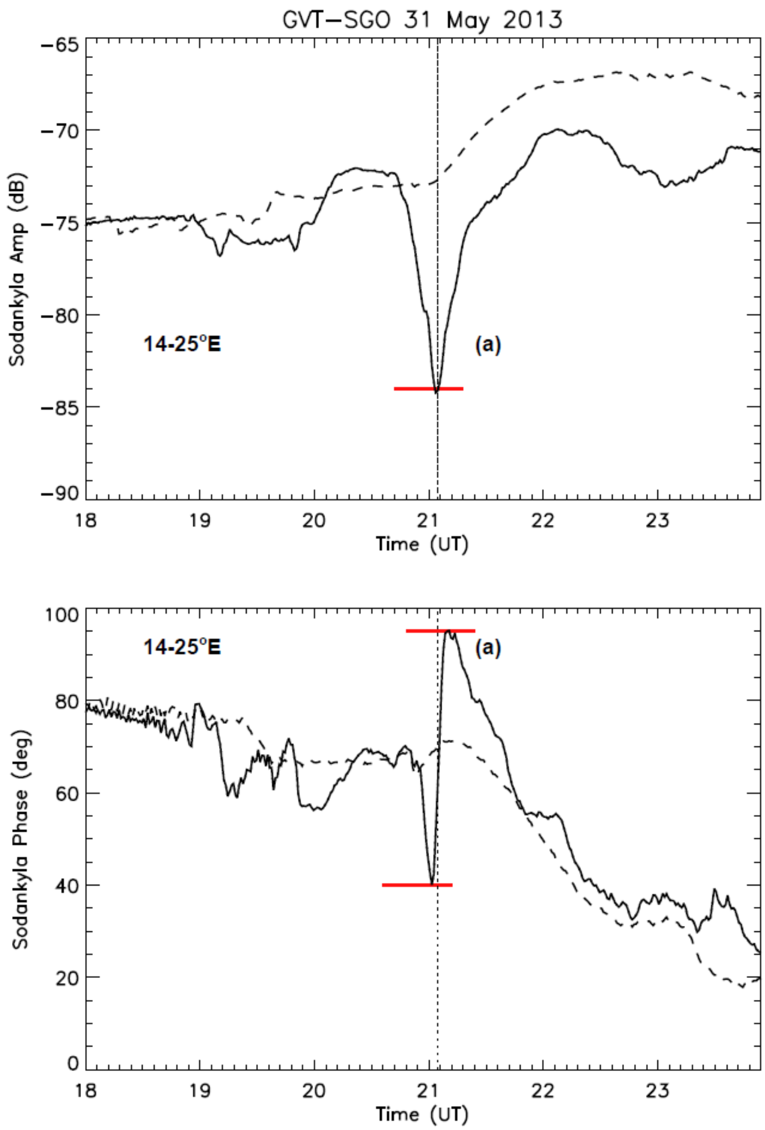

Figure 5. The variation of the amplitude and phase of the GVT transmitter (UK) received at Sodankylä, Finland along a path covering 2.5<*L*<5.3 on 31 May 2013. The longitude range over which the path crosses the *L*=4-5 contours (see Figure 1) is stated. The dashed line represents the variation observed during a typical non-disturbed day (02 June 2013). A large perturbation, labeled (a), is observed at 21 UT, co-incident with the EMIC IPDP wave observed at Oulu, Finland shown in Figure 3. Red bars indicate the maximum deviations.

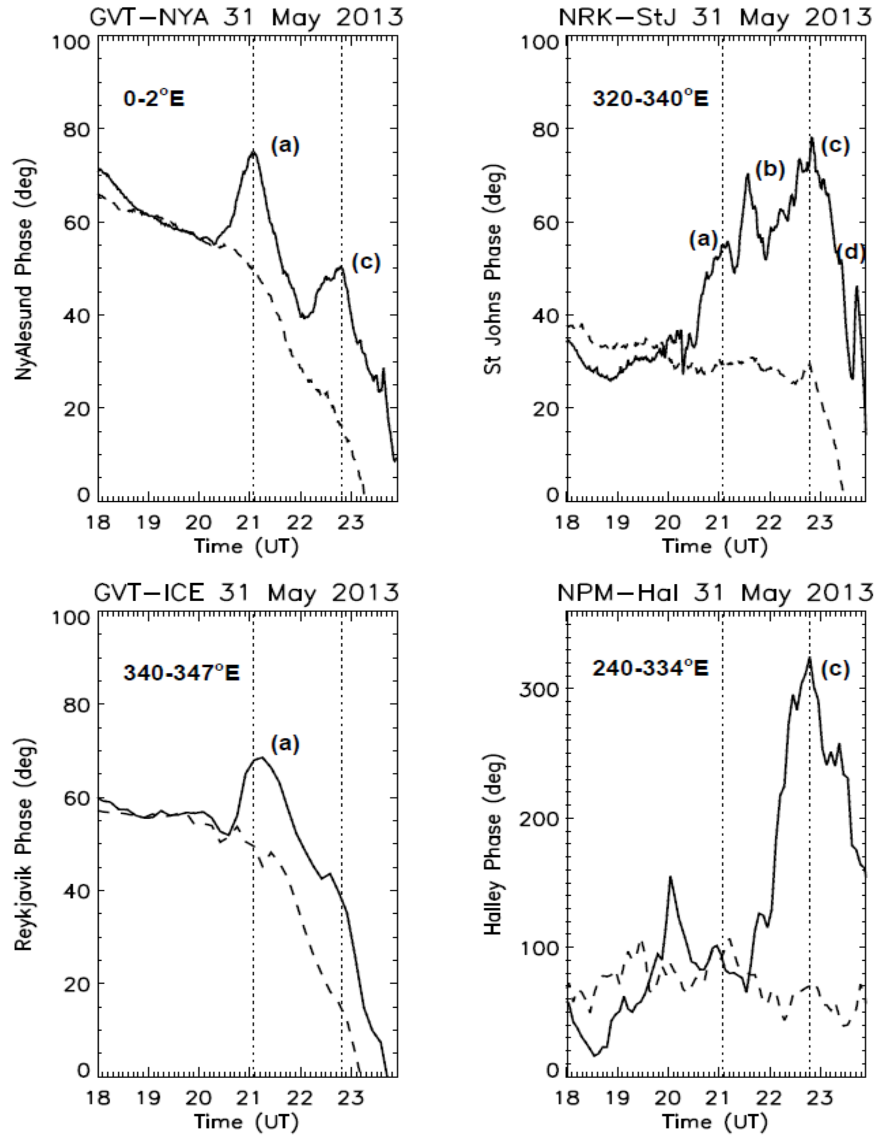

Figure 6. As Figure 5. The variation is shown of the phase of several transmitters received at four different locations. The two left-hand panels represent northern European paths, while the right-hand panels represent western-Atlantic paths. Vertical lines indicate the time of the most obvious phase perturbations, as well as the approximate times of EMIC waves observed on 31 May 2013 in northern Europe (21 UT) and western-Atlantic longitudes (22-23 UT). Perturbations observed are labeled (a) – (d). See text for more details.

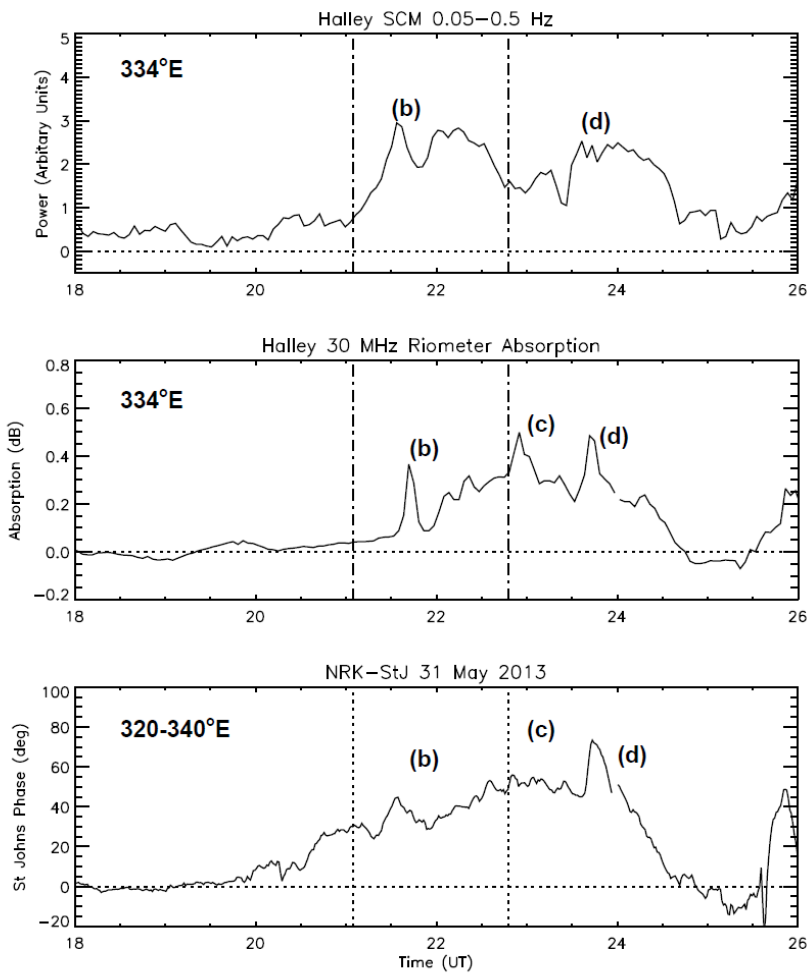

Figure 7. Upper panel. The power in the Pc1-2 wave band (0.05-0.5 Hz) observed by the search coil magnetometer at Halley, Antarctica during 31 May – 01 June 2013. Middle panel. The variation in the Halley riometer absorption. Lower panel. The phase perturbation observed on the Iceland NRK transmitter received at St. John's. Vertical dash-dot lines represent the times of peak electron precipitation observed in Figures 5 and 6. Perturbations are labeled as in Figure 6.

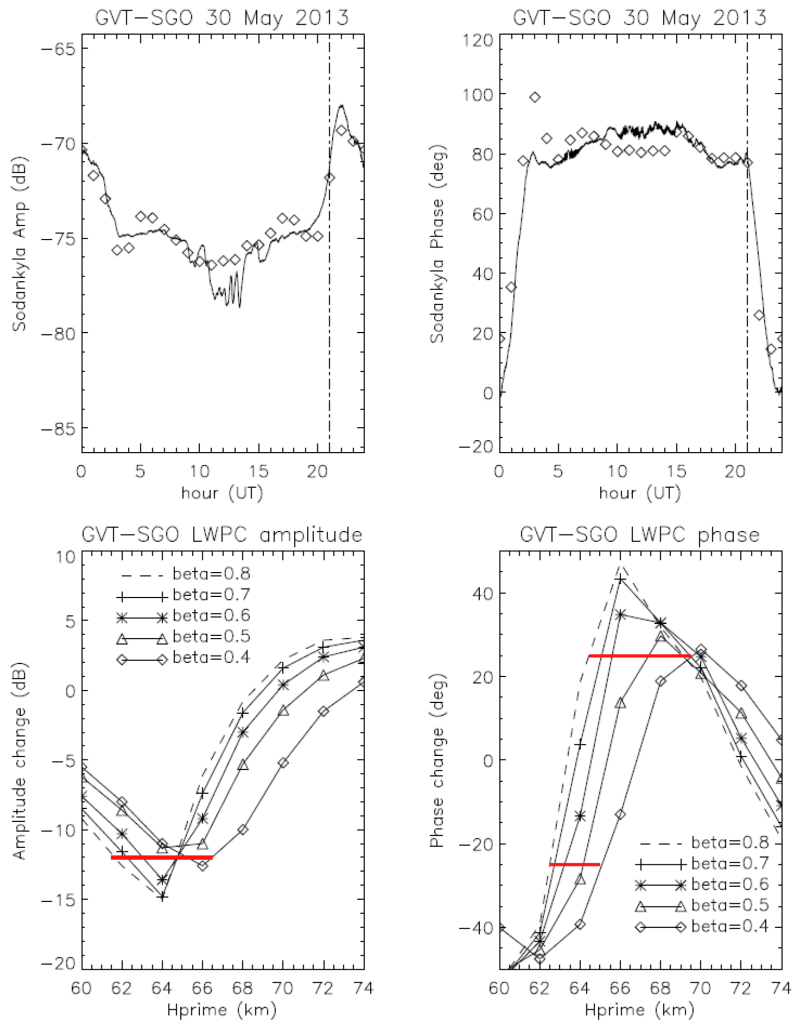

Figure 8. Upper panel. The observed amplitude and phase variation on a typical quiet-day (solid lines) for the UK-Finland propagation path, with LWPC modeling results for the same path and time of year (diamonds). A vertical dashed-dotted line at 21 UT represents the time of the EMIC precipitation event observed at Oulu, Finland. Lower panels. The LWPC phase and amplitude perturbations for a range of ionospheric sharpness values (β), where non-disturbed conditions are defined by the LWPC ionospheric model at 21 UT. Red bars represent the perturbation levels observed in Figure 5.

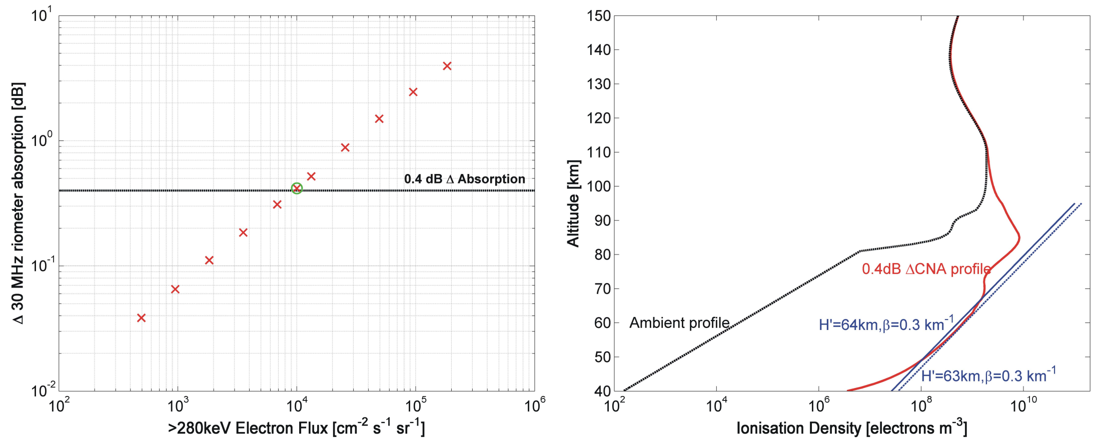

Figure 9. Left panel. The calculated change in 30 MHz riometer absorption (ΔCNA) at Halley at night for a range of flux magnitudes modeled with an energy range (280 keV – 5 MeV) and spectrum (*k*=-2.3) determined from analysis of event (b). The absorption with flux of 1 x 10^4 el. cm^{-2} s^{-1} sr^{-1} consistent with that reported by both the POES and the observed Halley riometer absorption for event (b) is picked out by the green circle. Right panel. The electron density profile above Halley. The ambient D-region ionosphere from 40-150 km is given by the black line, while the modified profile for the green circled point in the left hand panel is shown by the red line. The profiles for two representative Wait ionospheres are marked in blue.